Experimental and Theoretical Charge Density Distribution in Two Ternary Cobalt(III) Complexes of Aromatic Amino Acids

Jacob Overgaard,[†] Mark P. Waller,[‡] Ross Piltz,[§] James A. Platts,[||] Paul Emseis,[⊥] Peter Leverett,[⊥] Peter A. Williams,[⊥] and David E. Hibbs*,[‡]

Department of Chemistry, Aarhus University, Langelandsgade 140, DK-8000 Aarhus C, Denmark, Faculty of Pharmacy, University of Sydney, NSW 2006, Australia, Neutron Scattering Section, Australian Nuclear Science and Technology Organisation, PMB 1, Menai, NSW 2234, Australia, School of Chemistry, Cardiff University, Park Place, Cardiff CF10 3AT, U.K., and School of Natural Sciences, University of Western Sydney, Penrith South DC, NSW 1797, Australia

Received: December 15, 2006; In Final Form: March 16, 2007

The experimental charge density distributions in two optically active isomers of a Co complex have been determined. The complexes are Δ-α-[Co(*R*,*R*-picchxn)(*R*-trp)]$(ClO_4)_2 \cdot H_2O$ **(1)** and Λ-β_1-[Co(*R*,*R*-picchxn)-(*R*-trp)]$(CF_3SO_3)_2$ **(2)**, where picchxn is *N*,*N*′-bis(2-picolyl-1,2-diaminocyclohexane) and *R*-trp is the *R*-tryptophane anion. The molecular geometries of **1** and **2** are distinguished by the presence in complex **1** of intramolecular $\pi\cdots\pi$ stacking interactions and the presence in complex **2** of intramolecular hydrogen bonding. This pair of isomers therefore serves as an excellent model for studying noncovalent interactions and their effects on structure and electron density and the transferability of electron density properties between closely related molecules. For complex **2**, a combination of X-ray and neutron diffraction data created the basis for a X−N charge density refinement. A topological analysis of the resulting density distribution using the atoms in molecules methodology is presented along with d-orbital populations, showing that the metal−ligand bonds are relatively unaltered by the geometry changes between **1** and **2**. The experimental density has been supplemented by quantum chemical calculations on the cobalt complex cations: close agreement between theory and experiment is found in all cases. The energetics of the weak interactions are analyzed using both theory and experiment showing excellent quantitative agreement. In particular it is found that both methods correctly predict the stability of **2** over **1**. The transferability between isomers of the charge density and derived parameters is investigated and found to be invalid for these structurally related systems.

Introduction

Weak interactions such as hydrogen bonding and aromatic $\pi\cdots\pi$-stacking are abundant throughout nature, their importance in chemistry and biochemistry stemming from the additive effect of individual energies. In biochemical processes such as protein folding,[1] enzymatic activity,[2] and the structure of DNA, the number of weak intermolecular interactions is typically too numerous to enable their deconvolution and accurate investigation. This has provided the experimental impetus to create small molecular models with relatively few weak interactions for detailed investigation.[3] An increased understanding of these fundamental interactions in model systems may facilitate further understanding of real biological interactions and perhaps lead to biomimetic applications, for example in catalysis or pharmaceuticals. Molecular recognition and self-assembly are two emerging fields that are reliant upon such subtle interactions.[4] A more detailed understanding of the energetic and geometric properties of weak interactions would have widespread consequences for these fields of research.

The present study focuses on X−H$\cdots\pi$ hydrogen bonding in one and aromatic $\pi\cdots\pi$-stacking interactions in the other of two isomeric cobalt complexes that have been rationally designed to probe these weak intramolecular interactions. The complexes are Δ-α-[Co(*R*,*R*-picchxn)(*R*-trp)]$(ClO_4)_2 \cdot H_2O$ **(1)** and Λ-β_1-[Co(*R*,*R*-picchxn)(*R*-trp)]$\cdot(CF_3SO_3)_2$ **(2)**, where picchxn is *N*,*N*′-bis(2-picolyl-1,2-diaminocyclohexane), see Figure 1, and *R*-trp is the anion of *R*-tryptophane. The pcchxn ligand is believed to form a more thermodynamically stable β complex with Co(III) as previously observed with a wide variety of bidentate ligands[5] (see Figure 1b,c). However we note that the isolation and crystallization of **1** in the α form shows that thermodynamic stabilities of these diastereoisomers depend on subtle and small effects.

The cationic cobalt complexes in **1** and **2** are diastereoisomers, ensuring that the coordination spheres are as similar as possible and hence minimizing differences in steric and/or electronic effects. These isomers give rise to two different schemes of intramolecular interactions. In **1**, the aromatic indole group of the amino acid is almost parallel to one pyridine ring of the picchxn ligand, forming an aromatic $\pi\cdots\pi$ interaction. The ligand arrangement in **2** does not allow this situation to occur. Instead, there are two facial X−H$\cdots\pi$ interactions between the cyclohexyl portion of picchxn and the indole moiety of the tryptophan. As these model systems are structurally closely related, analysis of these interesting intramolecular interactions should be simplified.

* To whom correspondence should be addressed. E-mail: davidh@pharm.usyd.edu.au.
[†] Aarhus University.
[‡] University of Sydney.
[§] Australian Nuclear Science and Technology Organisation.
[||] Cardiff University.
[⊥] University of Western Sydney.

10.1021/jp068621n CCC: $37.00
Published on Web 09/18/2007

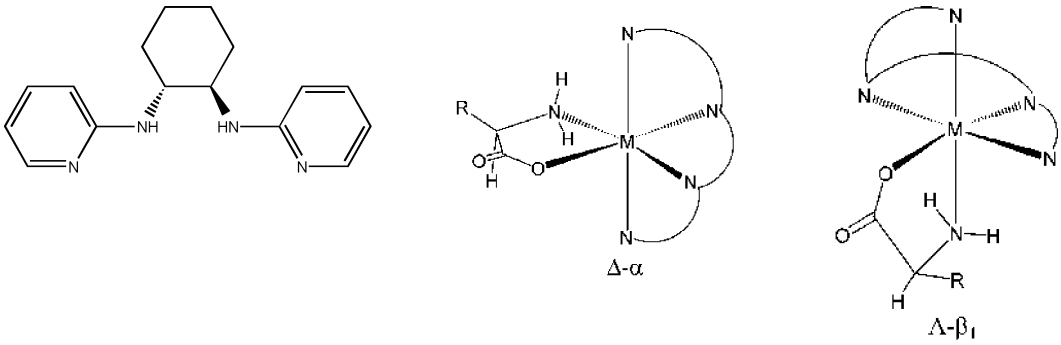

a b c

Figure 1. (a) Quadridentate *R*,*R*-picchxn ligand and the coordination topologies of (b) the Δ-α and (c) the Λ-β_1 complexes of Co(III) with *R*,*R*-picchxn and a bidentate amino acidate ligand.

Accurate location of the hydrogen atoms involved in hydrogen bonding is important to this investigation. The presence of the cobalt, with its associated relatively large scattering factor, makes the task of hydrogen location even more difficult from Fourier difference maps. Furthermore, with X-ray diffraction data it is in general not possible to model the anisotropic vibrations of hydrogen atoms; instead a simplified isotropic model is typically implemented.[6] Single-crystal neutron diffraction may resolve this problem, and thus, neutron diffraction was employed for both **1** and **2** to obtain accurate H atom positions and anisotropic thermal parameters. This combined X-ray and neutron approach (X−N method) has the added advantage that thermal motion is easier to deconvolute from the electron density, assuming that an effective temperature scaling scheme can be employed.

The atom-centered multipole formalism[7] is ideally suited for a quantitative investigation of the effects of isomerism and its influence on subtle intramolecular interactions. Within the quantum theory of atoms in molecules (QTAIM),[8] the concept of transferability has been studied extensively and it has been shown that essential properties such as the energy and multipole moments of an atom in a particular (open) system can indeed be transferred to another different system.[9] If the atomic charge distributions are in fact independent of their environment, which is the ultimate consequence of complete transferability, then it becomes possible to use these as building blocks in the construction of molecules. From the experimental point of view, it has been shown, using highly accurate high-resolution protein X-ray diffraction data, that it is in fact possible to perform a multipole description of the electron density distribution in proteins,[10] by using the previously determined amino acid charge densities compiled in a database,[11] instead of the regular spherical and noninteracting atoms.

The isomers **1** and **2** have previously been studied with NMR to assess their stability in solution.[3] This paper extends these studies and presents a detailed analysis of the experimental charge densities of **1** and **2**, augmented with quantum chemical calculations having particular emphasis on the weak intramolecular interactions.

Experimental Section

Crystal Preparation. Complexes **1** and **2** were prepared using a method previously described.[12]

X-ray Data Collection and Reduction. An orange single crystal of **1** ($0.25 \times 0.20 \times 0.20$ mm^3) was mounted using Paratone-N oil on a Bruker SMART 1000 CCD-based diffractometer at the University of Sydney. The experimental temperature was lowered to 100 K using an Oxford Cryocooling liquid-nitrogen device. X-ray diffraction data were collected using 0.3° Δω-scans maintaining the crystal-to-detector distance at 4.95 cm. Reciprocal space was covered by positioning the detector arm at three different setting angles in 2θ, −30, −60, and −100°, with corresponding exposure times, 10, 50, and 80 s/frame. A total of 1899 frames were collected for the low- and medium-angle data, while 1859 frames were measured at the high angle. The diffraction data was integrated using SAINT+,[13] and the unit cell parameters for **1** at 100 K were refined from 1011 reflections in the orthorhombic space group $P2_12_12_1$ with $Z = 4$, $F(000) = 1608$, and $\mu = 0.76$ mm^{-1} (Table 1). An empirical absorption correction was then applied using the program SORTAV[14] as implemented in the program-suite WinGX[15] ($T_{max} = 0.931$; $T_{min} = 0.727$). A total of 176 982 measured reflections were then merged using SORTAV, providing 51 461 unique reflections with an average redundancy of 3.4 up to $\sin(\theta)/\lambda = 1.249$ Å^{-1} with an overall completeness of 96.3%.

The X-ray experimental conditions for compound **2** were identical with the ones used for compound **1**; see above. From

TABLE 1: Crystallographic Details for 1 and 2

param	**1**	**2**
empirical formula	$C_{29}H_{37}Cl_2CoN_6O_{11}$	$C_{31}H_{35}CoF_6N_6O_8S_2$
fw	775.48	856.70
cryst size	0.25 × 0.20 × 0.20	0.25 × 0.25 × 0.20
cryst system	orthorhombic	triclinic
space group	$P2_12_12_1$	$P1$
a, Å	10.9327(15)	8.9008(4)
b, Å	12.7715(20)	9.8044(4)
c, Å	23.4475(37)	10.8095(5)
α, deg	90	78.221(3)
β, deg	90	82.243(3)
γ, deg	90	69.538(3)
V, Å^3	3273.9(1.1)	863.11(9)
no. of reflcns for cell refinement (θ_{min}, θ_{max}, deg)	1011 (3.31, 60.73)	1005 (2.25, 56.95)
$F(000)$	1608	440
T, K	100	100
ρ, g cm^{-3}	1.573	1.640
μ(Mo Kα), mm^{-1}	0.76	0.71
T_{max}, T_{min}	0.931, 0.727	0.886, 0.698
d_{min}, Å	0.40	0.42
N_{meas}, N_{uniq}	176 986, 51 461	54 594, 29 868
redundancy	3.3	1.7
completeness	0.963	0.622
no. discarded reflcns	8535	2778
h, k, l ranges	0/26, 0/31, −58/58	−19/20, −23/22, −25/25
R_{int}	0.025	0.012
N_{obs}, N_{var} (σ-cutoff)	42625, 995 (3)	28701, 699 (2)
$R_w(F)$, $R_w(F^2)$, >cutoff	0.023, 0.046	0.017, 0.035
$R(F)$, $R(F^2)$, all data	0.039, 0.036	0.019, 0.026
goodness of fit	1.30	1.51
max/min residual (<1.0 Å^{-1})	0.46/−0.43	0.39/−0.41

previous studies,[16] the space group is known to be *P*1. Therefore, to obtain the required redundancy as well as a good coverage of the reciprocal space, 17 series of frames (a total of 10 638 frames) were collected using a combination of ω- and ϕ-scans at four different swing angles (2θ), 90, 60, 25, and 0°, and with a crystal-to-detector distance of 4.987 cm. The exposure times were 80, 80, 50, and 10 s/frame, respectively. The diffraction data were integrated with SAINT+[13] from 1005 reflections. Subsequently, a face-indexed Gaussian absorption correction was performed ($\mu = 0.71$ mm^{-1}, $T_{max} = 0.886$, $T_{min} = 0.698$), and the 54 594 data were averaged with SORTAV[14] to give 29 868 unique reflections (Friedel pairs not merged; $R_{int} = 0.012$) with an average redundancy of 1.7 and overall completeness equal to 62.2%. Importantly however, the completeness of the data set below a $\sin(\theta)/\lambda$ threshold of 0.63 Å^{-1}, which is the region that contains the majority of the information about the valence electronic distribution, remains at 96.6%.

Neutron Data Collection and Reduction. The single-crystal neutron diffraction data was collected at a wavelength of 1.235(1) Å using the 2TANA four-circle diffractometer at the HIFAR reactor. Single crystals (**1**, 1.5 × 1.5 × 3 mm; **2**, 2 × 3 × 5 mm) were wrapped in aluminum foil, glued to aluminum sample pins, and mounted in the 2TANA closed-cycle helium refrigerator. The crystal was cooled to 100(2) K, and the intensities were collected and processed into integrated intensities using the ANSTO in-house programs DIFF, DIFFPLOT, and PEAKPOS. No significant trend was observed in the intensity of the two standard reflections, and so no time-dependent correction was applied to the data. A total of 5900 independent reflections for **1** in five shells of increasing Bragg angle up to a maximum of 90° were collected over a period of 27 days. A total 6935 independent reflections for **2** were measured over a 54 day period respectively in six shells of increasing Bragg angle up to a maximum of 105°. An analytical absorption correction was applied to the intensities, the correction varying from 21% to 27% for **1** and from 21% to 40% for **2**. Averaging equivalent and Friedel reflections of **1** gave 2913 unique reflections with *R*(merge) = 7.31%, and for **2** this procedure gave 3733 unique reflections with *R*(merge) = 4.87%. Structure refinement using no parameter constraints and with anisotropic thermal parameters for all atoms resulted for **1** in R1 = 6.35% and wR2 = 11.75% for a total of 770 parameters and for **2** in R1 = 2.44% and wR2 = 5.89% for a total of 803 parameters.

X−N Refinement. The quality of the neutron diffraction data for complex **1** was not sufficient to warrant a combined X−N refinement. Thus, the following paragraph is concerned with complex **2** only.

The crystal structure was solved independently with X-ray and neutron diffraction data using the procedure of direct methods coded in the program SHELXS.[17] The parameters included in the neutron refinement were atomic positions and anisotropic atomic displacement parameters (ADP's) for all atoms including hydrogen atoms, while the set of parameters employed in the X-ray IAM model consisted of atomic positions and anisotropic ADP's for all non-H atoms and hydrogen atoms treated as riding on the bonded atom with an isotropic thermal parameter derived from that particular neighboring atom.

After convergence of both models was achieved, an analysis of the two sets of ADP's of the non-hydrogen atoms was carried out using the program UIJXN.[18] This showed excellent agreement between non-H atom neutron and X-ray-derived ADP's (the mean value of the ratio U_{ii}(X) to U_{ii}(N) was 1.1(1)), which can be considered a sign of high accuracy of the X-ray structure factors. The detailed output of UIJXN as well as comments to it is available in the Supporting Information. This exercise indicated that the neutron-derived anisotropic ADP's for the hydrogens can be included in the refinement against X-ray data, thereby significantly improving the model. Furthermore, the hydrogen atom positions were adjusted to conform to the X−H bond distances from the neutron model and subsequently kept at these values. This final model was then imported into the charge density refinement package, XD.[19]

Charge Density Refinements. Both structures were solved from ab initio methods using SHELXS-86[17] and IAM models refined to convergence using SHELXL-97.[17]

The subsequent modeling of the experimental electron density in both compounds observed common guidelines. For both compounds, the resulting parameters from the IAM models were imported into the XD program package and their molecular electron density distributions (EDD) were described as a sum of pseudoatomic contributions using the Hansen−Coppens multipolar model.[7b] Neutral atomic scattering factors were used for all atoms, except for Co, which was described using the Co^{3+} scattering factor. These scattering factors were taken from Su and Coppens.[20] Due to the acentric nature of the space groups, extra care was taken in the inclusion of multipole parameters. The maximum level of multipoles reached was hexadecapoles for the Co and Cl atoms and octupoles for the remaining non-H atoms. Hydrogens were described using dipoles, common to similar types of hydrogen atoms. There are much more elaborate details of the charge density refinements to be found in the Supporting Information.

The refinements were continued until convergence and the Hirshfeld rigid bond test[21] was applied on the final models with positive results.

Computational Methods

Gas-phase calculations were performed using the Gaussian 03 suite of programs.[22] The hybrid BHandH functional[23] is combined with Pople's split valence basis set augmented with polarization and diffuse functions, namely 6-311++G(d,p)[24] and the Stuttgart Dresden ECP[25] for the cobalt center. We have recently shown that such an approach is able to reproduce high-level ab initio geometries and binding energies for the interaction of aromatic systems such as benzenes, pyridines, and DNA bases.[26] Second-order perturbation theory (MP2) was also employed on small model systems combined with the 6-311++G(d,p) basis.

Topological analysis of electron densities (ρ) was performed using the program XDPROP[19] (experiment) and the EXTREME[27] and AIM2000 packages[28] (theory). Integrated atomic properties were calculated from experimental densities using the program TOPXD.[29]

Results and Discussion

Molecular Structure. The coordination geometries for **1** and **2** are reported fully in the Supporting Information, while the Co−ligand geometries are also given in Table 2. ORTEP diagrams are shown in Figure 2.

There are some pronounced variations between the central parts of the two molecules. The bonds to the trp moiety are heavily distorted such that in **1** the Co−O bond is relatively longer than in **2**, while the opposite is the case for the Co−N(5) bond, to a smaller extent. On average, the Co−N bond lengths are similar. Also, the average deviation from octahedral coordination is the same for the two molecules (4.74° vs 4.88°). However, in **2** the two trans N−Co−N angles contribute

TABLE 2: Bond Distances and Angles in the CoL_6 Octahedron[a]

bond	d(**1**)	d(**2**)
Co(1)−O(1)	1.9214(3)	1.8918(3)
Co(1)−N(1)	1.9630(3)	1.9413(3)
Co(1)−N(2)	1.9486(3)	1.9228(3)
Co(1)−N(3)	1.9532(3)	1.9582(3)
Co(1)−N(4)	1.9277(3)	1.9443(3)
Co(1)−N(5)	1.9504(3)	1.9655(3)
angle	**−(1)**	**−(2)**
O(1)−Co(1)−N(1)	94.56(1)	178.73(1)
O(1)−Co(1)−N(2)	85.58(1)	96.08(1)
O(1)−Co(1)−N(3)	175.22(1)	93.30(1)
O(1)−Co(1)−N(4)	92.14(1)	85.79(1)
O(1)−Co(1)−N(5)	84.56(1)	85.38(1)
N(1)−Co(1)−N(2)	81.76(1)	84.03(1)
N(1)−Co(1)−N(3)	86.93(1)	86.55(1)
N(1)−Co(1)−N(4)	94.52(1)	92.94(1)
N(1)−Co(1)−N(5)	176.30(1)	95.89(1)
N(2)−Co(1)−N(3)	99.14(1)	170.34(1)
N(2)−Co(1)−N(4)	175.46(1)	95.35(1)
N(2)−Co(1)−N(5)	94.59(1)	89.64(1)
N(3)−Co(1)−N(4)	83.21(1)	83.04(1)
N(3)−Co(1)−N(5)	94.23(1)	93.40(1)
N(4)−Co(1)−N(5)	89.10(1)	170.27(1)

[a] d(**1**) and d(**2**) are the bond lengths in **1** and **2**, respectively, in Å, and the angles −(**1**) and −(**2**) are given in deg.

significantly more to the deviation than they do in **1**. The overall impression to convey is that the complexes **1** and **2** exhibit quite altered bonding environments, which we now study in more detail using the electron density.

Electron Density. Co−Ligand Bonding Environment. We now turn to the electron density and the task of establishing the extent to which isomerism creates a different electronic environment around the cobalt center. As seen above, the bonding geometries about Co differ substantially between **1** and **2**. Static deformation density maps in two perpendicular planes, both approximately including Co and four ligands, are shown in Figure 3 for **1** (the corresponding maps for **2** show highly similar features and are thus not presented). Figure 3 show accumulation of density between Co−ligand bonds and smaller depletion of charge in the bonding directions close to Co. Lone pairs on the ligand atoms are directed toward the central Co atom, as expected. Static model deformation density maps of the ligand and solvent molecules do not portray any unusual features.

To get an overview of the redistribution of electron density due to bonding that has occurred around the central Co atom, it is advantageous to view this density in three dimensions. Thus, Figure 4 shows the static model deformation density for both complexes **1** and **2** in a region centered on Co. First of all, we find that charge has accumulated near the corners of a cube centered on Co. The maxima in this density are located such as to be furthest away from any metal−ligand bond. However, in both complexes this symmetry is clearly not present in the upper corner facing toward the viewer. In **1**, the two maxima have even merged to one broad maximum, while, in **2**, one maximum is much lower in magnitude (and therefore not visible in Figure 4b due to the choice of isosurface value).

The accumulation of charge is even better visualized in the 3D isosurface plot of the Laplacian function—a function that

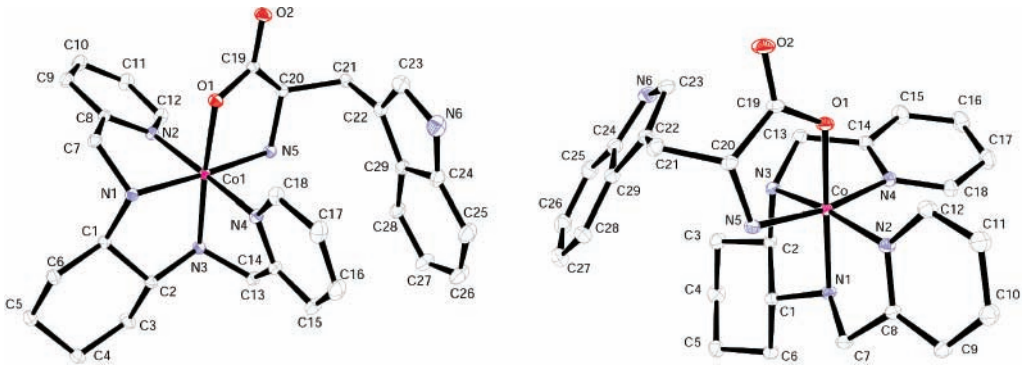

Figure 2. ORTEP diagrams showing the thermal ellipsoids at 50% probability level for **1** (left) and **2** (right). Hydrogen atoms and the solvent molecules have been omitted for clarity.

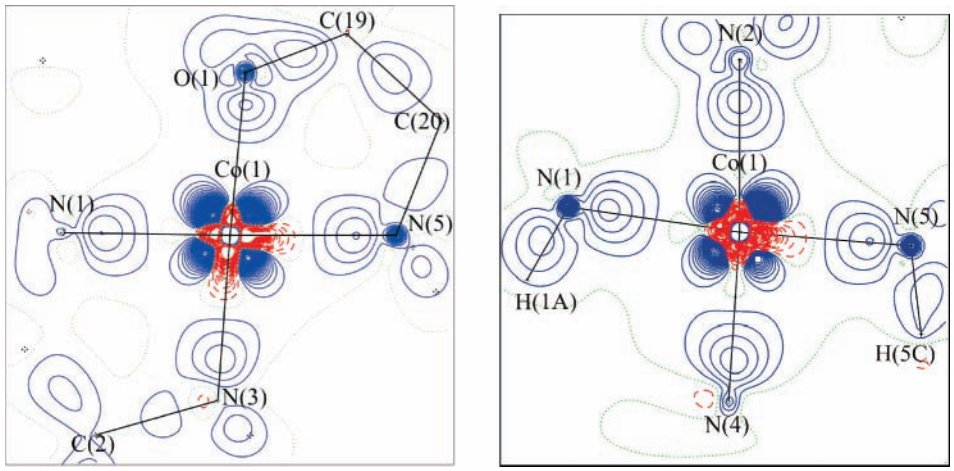

Figure 3. Static model deformation density maps of the planes containing (left) the central O(1)−Co−N(5) and (right) the N(1)−Co−N(2) in **1**. Contours are shown at ±0.20 e Å^{-3}. The atoms C(19), C(20), and C(2) are all partly out of the shown planes. Therefore, the bonds involving these atoms are not accurately depicted in these plots.

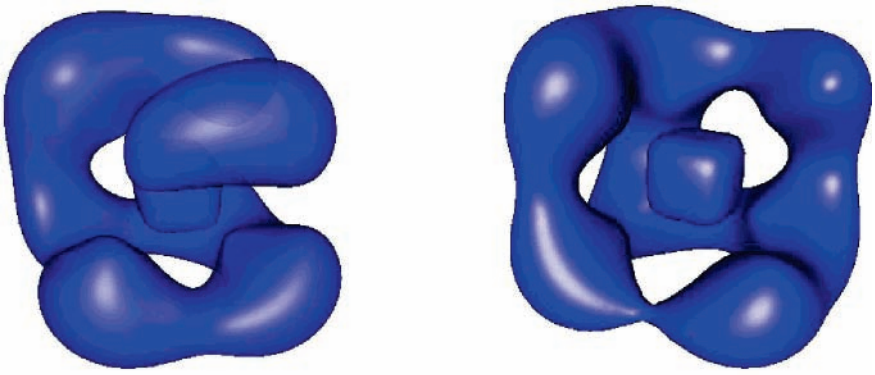

Figure 4. Isosurface mapping in the region close to Co for **1** (left) and **2** (right). The isosurface is rendered at a value of the static model deformation density of 3.0 e Å^{-3}.

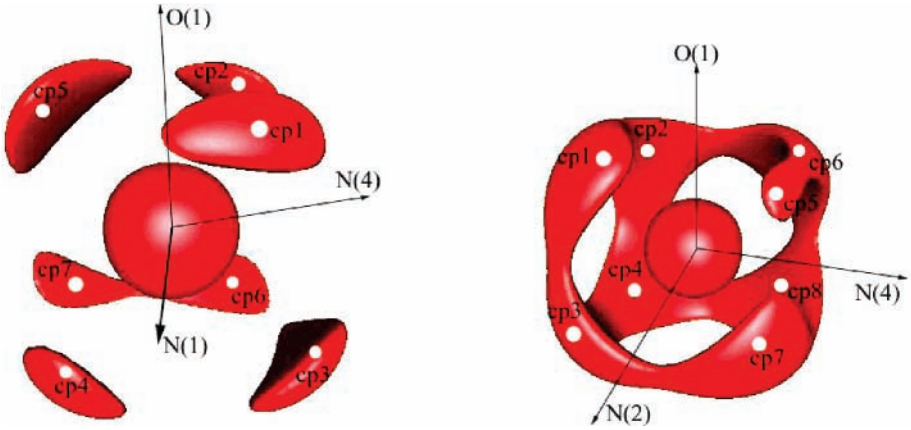

Figure 5. Isosurface mapping of the Laplacian function in the region close to Co for **1** (left) and **2** (right). The isosurface is rendered at a value of the Laplacian of the electron density of −2250 e Å^{-5} for **1** and −1600 e Å^{-5} for **2**. The coordinate systems show the directions to three ligands. The orientation is similar to the one displayed in Figure 4.

TABLE 3: Properties of the Valence Shell Charge Concentrations around Co[a]

CP no.	r_{Co-CP}(**1**)	ρ_{CP}(**1**)	$\nabla^2\rho_{CP}$(**1**)	r_{Co-CP}(**2**)	ρ_{CP}(**2**)	$\nabla^2\rho_{CP}$(**2**)
1	0.294	34.9	−2	0.295	33.9	−2587
2	0.293	35.1	−2	0.295	35.9	−2532
3	0.291	37.6	−3	0.293	35.8	−2832
4	0.294	35.2	−2	0.293	37.0	−2733
5	0.291	37.8	−3	0.306	26.7	−1592
6	0.295	34.9	−2	0.295	34.4	−2552
7	0.295	34.5	−2	0.296	33.6	−2463
8				0.294	35.6	−2652

[a] Units used: r, Å; ρ, e Å^{-3}; $\nabla^2\rho$, e Å^{-5}.

peaks in regions where the concentration of the electron density is higher than in the surrounding regions. This plot is shown in Figure 5. The peaks, i.e., the density accumulations, are found in the corners of a cube centered on Co and the Co−ligand connection lines extending through the midpoints of the faces of the cube. The exact positions and the topological properties of the density at these points can be found by first locating the critical points in the Laplacian function; see Table 3 and Figure 5.

The results, the valence shell charge concentrations or VSCCs, all show very similar properties, except for CP5 in **2**. This VSCC is significantly further from Co and has much lower density and higher Laplacian than all other VSCCs. It is conspicuous that the CP's with dissimilar properties are both on the same side as O(1) above the Co−N_4 plane spanned by the piccxhn group and opposite the indole group of the trp. The carboxylate group of trp is quite electron withdrawing and may be the cause of the change in electron density.

d-Orbital Populations. To expand the analysis of the Co−ligand bonding environment, metal d-orbital population analysis provides a useful tool. Experimental d-orbital populations can be derived from the population parameters used in the multipole model. In the refinement procedure (see Experimental Section), it was assumed that the 4s orbitals on the Co atoms are unoccupied, leaving the 3d orbitals to participate in bonding. It is therefore straightforward to derive the relationship between the refined P_{lmp} and the d-orbital populations.[30] Recently, a method was developed for estimating the influence on the derived d-orbital populations from the definition of the local coordinate system.[31] Applying this program to **1** and **2** shows the expected similar results for both compounds, namely, that the axes point toward the ligands.

Table 4 shows d-orbital populations in broad agreement with the nominal d^6 configuration of Co^{3+}, with three doubly occupied t_{2g} orbitals (d_{xy}, d_{xz}, and d_{yz}). The slightly decreased population (i.e., less than 2.00) in the t_{2g} orbitals could be a sign of σ donation. In addition, both e_g orbitals exhibit significant

TABLE 4: d-Orbital Populations on Co

compd (% populatn)	d(z^2)	d(x^2-y^2)	d(yz)	d(xy)	d(xz)	SUM
1 (%)	**0.75(2) (9.2)**	**0.84(2) (10.3)**	**2.04(2) (25.0)**	**2.03(2) (24.9)**	**2.52(2) (30.9)**	**8.16**
2 (%)	**0.37(2)** (5.1)	**0.96(2)** (13.1)	**1.79(2)** (24.5)	**2.16(2)** (29.5)	**2.03(2)** (27.8)	**7.31**

TABLE 5: Topological Analysis of the Cation (First Line, 1; Second Line, 2)

bond	ρ_{bcp}	$\nabla^2\rho_{bcp}$	ϵ	d_{1-2}	d_{1-bcp}	$-\lambda_1$	$\lambda_1+\lambda_2$	λ_3	$-V$	H	G/ρ
Co−O(1)	0.549(5)	18.27(1)	0.32	1.922	0.927	2.17	−3.82	22.09	1.02	0.13	2.09
	0.612(3)	17.46(1)	0.40	1.901	0.906	2.58	−4.42	21.88	1.12	0.05	1.91
Co−N(1)	0.662(5)	15.36(1)	0.23	1.966	0.923	2.91	−5.27	20.64	1.17	−0.05	1.69
	0.570(4)	14.34(1)	0.34	1.944	0.912	2.08	−3.62	17.96	0.96	0.02	1.73
Co−N(2)	0.742(5)	15.02(1)	0.35	1.949	0.926	4.10	−7.14	22.16	1.33	−0.14	1.60
	0.728(5)	14.17(1)	0.44	1.929	0.917	4.16	−7.04	21.21	1.28	−0.14	1.56
Co−N(3)	0.640(5)	15.15(1)	0.42	1.954	0.924	2.88	−4.91	20.06	1.12	−0.03	1.70
	0.691(4)	13.79(1)	0.13	1.958	0.931	3.26	−6.15	19.93	1.19	−0.11	1.56
Co−N(4)	0.774(5)	16.16(1)	0.35	1.928	0.913	4.12	−7.17	23.34	1.43	−0.15	1.65
	0.662(5)	15.65(1)	0.28	1.945	0.915	2.73	−4.85	20.49	1.17	−0.04	1.71
Co−N(5)	0.658(5)	15.38(1)	0.05	1.953	0.920	2.63	−5.14	20.52	1.16	−0.04	1.70
	0.643(4)	13.76(1)	0.16	1.972	0.930	2.79	−5.19	18.94	1.09	−0.06	1.60

TABLE 6: Experimentally Derived Atomic Charges[37]

	1			**2**		
Atom	$q(P_v)$	$q(\Omega)$	$V(\Omega)$	$q(P_v)$	$q(\Omega)$	$V(\Omega)$
Co	+0.84	+0.86	46.5	+1.69	+0.95	48.5
O(1)	−0.75	−1.27	95.0	−0.72	−1.30	95.6
N(1)	−0.85	−1.02	61.1	−0.55	−0.71	53.3
N(2)	−0.52	−1.11	76.1	−0.47	−1.02	68.8
N(3)	−0.67	−0.92	61.0	−0.55	−0.75	55.9
N(4)	−0.50	−1.27	76.2	−0.63	−1.23	70.3
N(5)	−0.74	−1.18	74.7	−0.69	−1.16	68.8
CoL_6	−3.19	−5.91	490.6	−1.92	−5.22	461.2

occupation—the equatorial $d_{x^2-y^2}$ more than the axial d_{z^2}—signifying back-donation from all six ligands to the Co center to some extent.[32] Thus, with the Co−O(1) defining the *z*-axis, d-orbital populations indicate that back-bonding in Co−O(1) and in the Co−N bond trans to this may be weaker than the back-donation from the four equatorial Co−N bonds.

Topological Analysis of the Electron Density. A quantitative comparison of whether or not the Co−ligand bonds differ between isomers can be found from a topological analysis of the total electron density distribution. Table 5 contains the results of such analysis for the Co−ligand bonds only. This shows that the Laplacian is positive for all bonds, indicating charge depletion in the interatomic regions and, hence, largely electrostatic interactions. Also, ρ_{bcp} is smaller and $\nabla^2\rho_{bcp}$ more positive for Co−O than for any Co−N bond, despite the fact that the Co−O bonds are slightly shorter. A closer look points to the perpendicular curvatures ($\lambda_1 + \lambda_2$) and not the curvature along the bond (λ_3) as the origin of this difference. The Co−N bonds exhibit broadly similar properties within each molecule, and no obvious difference between **1** and **2** is apparent.

In general, a positive value of $\nabla^2\rho_{bcp}$ is a fingerprint of a closed-shell or electrostatic interaction. However, recent work has shown that the energy density distribution may be a more sensitive tool in its description of bonding effects in weak interactions or in regions with little charge accumulation,[33] such as metal−ligand bonds. Thus, Table 5 reports also potential and kinetic energy densities, calculated using Abramov's semiempirical formula.[34] Experimental work by Macchi et al.[35] on metal−carbonyl complexes showed that covalent interactions are characterized by dominance of the potential energy density (i.e., $-V_{bcp} > G_{bcp}$) such that the total energy density becomes negative $H_{bcp} < 0$, along with a small $G(r_{bcp})/\rho_{bcp}$ ratio.

Using such definitions, the Co−O bonds in **1** and **2** having positive values of *H* appear more electrostatic in nature, whereas most Co−N bonds have H_{bcp} less than or close to zero and hence possess more covalent character. Two interesting cases are Co−N(3) in **1** and Co−N(1) in **2**, which have noticeably less covalent character as measured by H_{bcp} than the other Co−N bonds and are also among the lowest ρ_{bcp} found. The fact that both these bonds are trans to the Co−O bond suggests that this observation is the result of an induced trans-effect.

The electron density with its Laplacian around the Co atom is ultimately a function of the d-orbital population on Co. In a perfect octahedral coordination, d-orbitals split into energetically favored (t_{2g}) and disfavored (e_g) sets: Co^{3+} ion has six d-electrons, which in the presence of a large ligand field should fully occupy the three t_{2g} orbitals. The greater back-donation from the equatorial ligands ($d_{x^2-y^2} > d_{z^2}$) corresponds well with the topological analysis in that the two axial bonds from Co show the smallest values of ρ_{bcp}.

Atomic Charges. QTAIM provides an unambiguous boundary for an atomic basin and, hence, a natural definition of atomic charge as the electron density integrated within this basin. An alternative definition comes from refined monopole populations: $q = N - P_v$, where *N* is the number of valence electrons and P_v is the population.[36] Table 6 lists the integrated experimental atomic charges using both definitions of this property for selected atoms. Both definitions agree on the general picture of a positive Co atom surrounded by negative ligand atoms but differ on the details. Co is slightly more positive in **2** than in **1** and charges on N show more variation in **2**, varying from −0.71 to −1.23 e, whereas in **1** a smaller range of 0.36 e is found.

The overall volumes of the CoL_6 parts differ by approximately 6%, which is due to different basin volumes of the N atoms. These basins are systematically smaller in complex **2** for all N atoms, which also reflect in their integrated atomic charges that sum to almost one full electron less. A similar trend is found in the monopole charges. However, assigning this to the presence

TABLE 7: Atomic Charges from Theoretical Natural Population Analysis

	$q(\Omega)$	
atom	**1**	**2**
Co	+1.22	+1.22
O(1)	−0.78	−0.78
N(1)	−0.65	−0.67
N(2)	−0.54	−0.54
N(3)	−0.67	−0.75
N(4)	−0.55	−0.53
N(5)	−0.85	−0.83
CoL_6	−2.81	−2.88

of a systematic error of some sort is not straightforward since (1) both atoms Co and O(1) are nearly identical and (2) the convergence of the basin integration was in all cases satisfactory. Instead, a possible explanation could be the different geometries of the two isomers and subsequent different bonding schemes. An additional explanation could be the different packing schemes.

DFT calculations were also employed to carry out natural population analysis,[38] to compare atomic charges with those obtained from the multipole refinement: these are reported in Table 7. Charges are generally smaller than QTAIM-derived values and more comparable to those generated from monopole populations in Table 6. Overall, theoretical values are more similar between **1** and **2** than was found experimentally—charges on Co, O(1), and N(2) are identical in both cations, while those on N(1), N(4), and N(5) are within 0.02 e. Only N(3) shows a large variation between isomers, being 0.08 e more negative in **2** than in **1**. This is perhaps due to the fact that N(3) is trans to O(1) in **1** but cis to this atom in **2**, although such a difference is not evident in N(1), the atom trans to O(1) in **2**. This theoretical analysis therefore suggests that the large differences in atomic charges between **1** and **2** reported in Table 6 are not inherent to the coordination geometry and may be due to to subtle differences in either the refined multipole parameters or crystal packing effects.

Similarity of Electron Densities. The cationic complexes in **1** and **2** are stereoisomers; they make an ideal test of the transferability of charge distributions and related parameters, a topic of considerable current interest.[9−11] Inspection of the 513 refined multipole population parameters show an average discrepancy between **1** and **2** in absolute values of 0.08, a value that should be compared to an average esd of the multipoles of 0.02−0.03.[39] For multipoles with absolute populations larger than 0.1, the discrepancy is slightly larger at 0.10, and for monopoles, only a difference of 0.07 is found. On the basis of these findings, it could be argued that multipole parameters are not transferable across isomers, However, the full multipole model used in these studies is highly flexible and it may happen that two or more independent sets of population parameters provide equivalent refinement statistics;[40] thus, an analysis of the properties of the resulting charge densities instead of the multipole parameters themselves is worthwhile.

Popelier and co-workers[41] have set out a measure of molecular similarity and transferability on the basis of topological analysis of the electron density, termed quantum topological molecular similarity (QTMS). In analogy with this approach, we have compared topological parameters for **1** and **2**, using values in each bond of ρ_{bcp}, $\nabla^2\rho_{bcp}$, d_{1-bcp}, and ϵ, and combined them according to the following formula:

$$\langle d \rangle = \sum_{i=1}^{n_{bond}} (d_i/(4n_{atom}))$$

Here

$$d_i = \sqrt{(\rho_1 - \rho_2)^2 + (\nabla^2\rho_1 - \nabla^2\rho_2)^2 + (d_1 - d_2)^2 + (\epsilon_1 - \epsilon_2)^2}$$

The result was a $\langle d \rangle$ value of 0.77, which is in same order of magnitude as the result given in the original paper[41] for the difference between *p*-NH_2 and *p*-NO_2 benzoic acid of 0.37. However, our relatively small number (0.77) hides large fluctuations, mainly caused by the differences in $\nabla^2\rho_{bcp}$, which have a tendency to dominate the value of d_i. The largest d_i is 15.1 for the O(2)−C(19) bond, followed by d_i values around 9 for the other C−O bond and the N(4)−C(14). It is worth noticing that, in both of the C−O bonds, the position of the bcp is similar for **1** and **2**, while in the N(4)−C(14) bond this is not the case; it has moved 0.05 Å closer to N(4) in **2**. Thus, the comparison of the bonds in bcp space corroborates the findings from the crude comparison of the population parameters that the transferability of atomic properties is not straightforward.

Weak Interactions. Hydrogen Bonds: Experimental Results. The crystalline samples are maintained by a number of hydrogen bonds (HB's) linking the counterions and solvent molecules to the Co complexes. One noteworthy difference in the hydrogen bond pattern between **1** and **2** is that the carbonyl-oxygen O(2) is involved in a strong HB in **1** (N(5)−H(5D)···O(2)), while O(2) in **2** only interacts very weakly with three relatively remote aromatic C−H groups. On the other hand, in **2** there are four relatively strong HB's to the CF_3SO_3 solvent molecule, which account for the majority of the stabilization of this crystal structure. Overall, the HB pattern is more pervasive in **2**. The topological properties of these weak interactions are summarized in Tables 8 and 9.

In addition to these *inter*molecular HB's, which all can be categorized as normal to weak, there are a number of weak *intra*molecular interactions. In **1**, H(5C) is located in the region between the aromatic indole and pyridine ring systems, and the opportunity exists for a N−H···π interaction concurrently with a π···π stacking interaction. The molecular arrangement in **2** does not allow this situation to occur. Instead, there are two facial X−H···π interactions between N(3)−H(03), C(3)−H(3A), and the indole ring system.

In **1**, no bcp is found between H(5C) and any atom involved in the π-system. However, there is a bond critical point between this H(5C) and H(28), which is part of the indole system. Such H···H contacts have been studied in details by Matta et al., who found them to be common in a range of cyclic hydrocarbon molecules and characterized them as attractive bonding interactions.[42]

Similarly, two bcp's are found between the two π-systems in **1**. The region between the two π-systems is characterized by a rather low and flat charge density, which an atom-centered description may not be perfectly suited to describe. Thus, it requires extra care to locate the best model. However, the number of inter-ring bcp's has not been observed to depend on the multipole model used. Moreover, the motif of two bcp's found in the region between rings was repeatedly found in recent ab initio and DFT theoretical studies of π-stacking.[26]

In **2**, bcp's corresponding to both of the aforementioned H···π interactions are located. The bond paths (Figure 6) show curved bonds with the midpoint of a C═C bond apparently acting as one of the attractors, although the bond path turns toward one of the nuclei just before touching the bond midpoint due to the fact that a bond path by definition starts and ends on a nucleus ((3,−3) bcp).

TABLE 8: Topological Analysis of the Weak Inter- and Intramolecular Interactions in 1[a]

bond	ρ_{bcp}	$\nabla^2\rho_{bcp}$	R_{1-2}	L_{bp}	d_{1-bcp}	$-\lambda_1$	$-\lambda_2$	λ_3	V	H	E
N(6)−H(6)···O(5)[i]	0.12	2.59	1.96	1.96	0.70	0.56	0.53	3.68	−0.11	0.04	21.3
N(5)−H(5D)···O(2)[ii]	0.17	3.32	1.86	1.86	0.65	0.84	0.78	4.94	−0.16	0.03	31.0
O(1W)−H(1W)···O(2)[ii]	0.10	3.31	1.87	1.99	0.65	0.62	0.41	4.34	−0.11	0.06	21.3
O(1W)−H(2W)···O(5)[iii]	0.07	1.75	2.03	2.32	0.82	0.38	0.26	2.40	−0.06	0.03	11.7
N(5)−H(5C)···H(28)	0.06	0.94	2.17	2.57	1.00	0.24	0.13	1.31	−0.04	0.01	7.9
$\pi\cdots\pi$(1)	0.03	0.34				0.08	0.03	0.45	−0.01	0.01	2.1
$\pi\cdots\pi$(2)	0.03	0.29				0.06	0.01	0.36	−0.01	0.00	2.1
C(13)−H(13A)···H(28)	0.03	0.32	2.89		1.32	0.06	0.04	0.42	−0.01	0.01	2.1
H(20)···H(12)	0.04	0.54	2.61		1.18	0.19	0.08	0.80	−0.02	0.01	2.1
C(18)−H(18)···O(1)	0.08	1.26	2.41		1.03	0.35	0.28	1.88	−0.05	0.02	9.7

TABLE 9: Topological Analysis of the Weak Hydrogen Bonds in 2[a]

bond	ρ_{bcp}	$\nabla^2\rho_{bcp}$	R_{1-2}	L_{bp}	d_{1-bcp}	$-\lambda_1$	$-\lambda_2$	λ_3	V	H	E
N(1)−H(01)···O(04)[i]	0.16	3.00	1.92	1.95	0.65	0.74	0.67	4.42	−0.14	0.03	27.2
N(6)−H(06)···O(03)[i]	0.11	2.65	1.95	2.08	0.77	0.55	0.41	3.61	−0.10	0.04	19.2
N(5)−H(05A)···O(06)	0.14	3.20	1.93	1.93	0.64	0.66	0.50	4.36	−0.14	0.04	27.2
N(5)−H(05B)···O(01)[ii]	0.17	1.37	2.19	2.40	0.88	0.83	0.67	2.87	−0.11	−0.01	21.3
C(15)−H(15)···O(2)[i]	0.03	0.52	2.87	3.16	1.33	0.12	0.10	0.74	−0.02	0.01	3.8
C(16)−H(16)···O(2)[i]	0.04	0.60	2.76	2.95	1.28	0.15	0.13	0.88	−0.02	0.01	3.8
C(9)−H(9)···O(2)[ii]	0.07	1.31	2.25	2.29	0.90	0.28	0.24	1.83	−0.05	0.02	9.7
C(3)−H(3A)···C(25)	0.08	0.73	2.72	3.25	1.15	0.24	0.10	1.07	−0.04	0.01	7.9
N(3)−H(03)···C(23)	0.07	1.05	2.48	2.79	0.92	0.29	0.16	1.49	−0.04	0.01	7.9
C(13)−H(13B)···C(23)	0.04	0.51	2.85	3.04	1.23	0.15	0.09	0.75	−0.02	0.01	3.8
C(23)−H(23)···O(2)	0.04	0.66	2.63	2.72	1.11	0.20	0.11	0.97	−0.02	0.01	3.8
C(18)−H(18)···N(2)	0.07	0.88	2.10	2.40	1.10	0.34	0.24	1.46	−0.04	0.01	7.9
C(1)−H(1)···H(05B)	0.07	1.16	2.50	2.64	1.09	0.24	0.10	1.51	−0.05	0.02	9.7

[a] Units: ρ_{bcp}, e Å^{-3}; $\nabla^2\rho_{bcp}$, λ_i, e Å^{-5}; R_{1-2}, L_{bp}, d_{1-bcp}, Å; G, H, hartree au^{-3}; E, kJ mol^{-1}. L_{bp}: Length of bond path. Atom key: (i) $1 + x, y, z$; (ii) $x, 1 + y, z$.

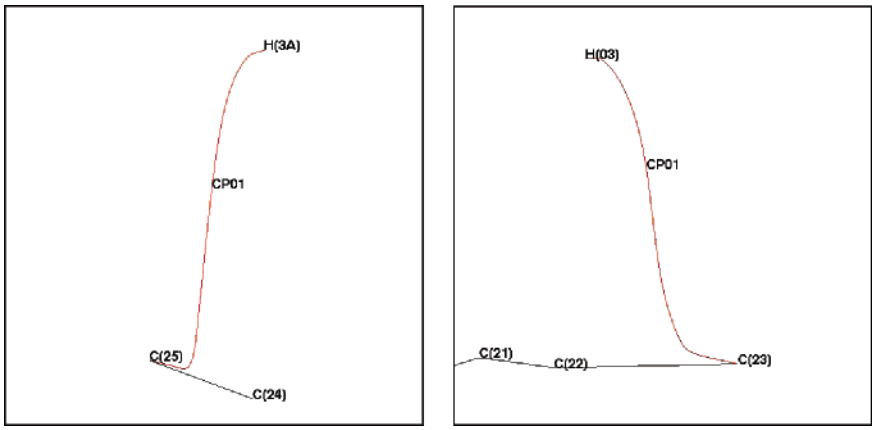

Figure 6. Bond paths in the two X−H···π bonds in **2**.

It is possible to experimentally estimate the energies of weak interactions such as HB's using the topological analysis of the electron density, as suggested by Espinosa et al.[43] The bond energies found using this approach are also given in the Tables 8 and 9.

Energetics of Weak Intramolecular Interactions: Theoretical Results. Gas-phase DFT calculations at crystallographic coordinates (solvent and counterions not included in the calculations) of **1** and **2** were employed to evaluate the relative energy of **1** and **2**. The BHandH functional combined with the SDD effective core potential and basis set for Co and 6-311++G-(d,p) for the remaining atoms indicate that **2** is 12.3 kJ mol^{-1} more stable than **1**; i.e., complex **2** containing intramolecular H-bonds is more stable than complex **1** with intramolecular $\pi\cdots\pi$ stacking (Figure 7). This single value does not offer much chemical insight: a more interesting question is the origin of this difference in energy, i.e., if the weak interactions discussed above solely responsible. The theoretical and experimental charge density was therefore analyzed to help answer this question.

To investigate the properties and energies of the different intermolecular interactions in **1** and **2**, topological analysis of the DFT derived density was performed. In **1**, three bcp's are located corresponding to π-stacking interactions between pyridine and indole π-systems, linking C(14), C(15), and C(16) with C(28), C(27), and C(26), respectively. We also find a C−H···π interaction linking C(13) with C(28) from a CH_2 group of picchxn to indole. In addition, C(18)− H(18)···O(1) form a hydrogen bond, as do C(20)−H(20)···C(12).

In **2**, the theoretical topological analysis locates exactly the same weak interactions as reported in Table 9. In the latter (see text for more details) BCPs are displayed as red spheres.

As well as locating the nonbonding interactions in **1** and **2**, topological analysis can be used to estimate the strengths of the interactions. The value of the electron density at the H-bond critical point has long been used to estimate the energy of such interactions, and we recently constructed a similar method for π-stacking.[26] Applying these estimations to **1** and **2**, we find that the total energies of nonbonded interactions are 23.5 and 29.7 kJ mol^{-1}, respectively. In **1**, π-stacking contributes 13 kJ

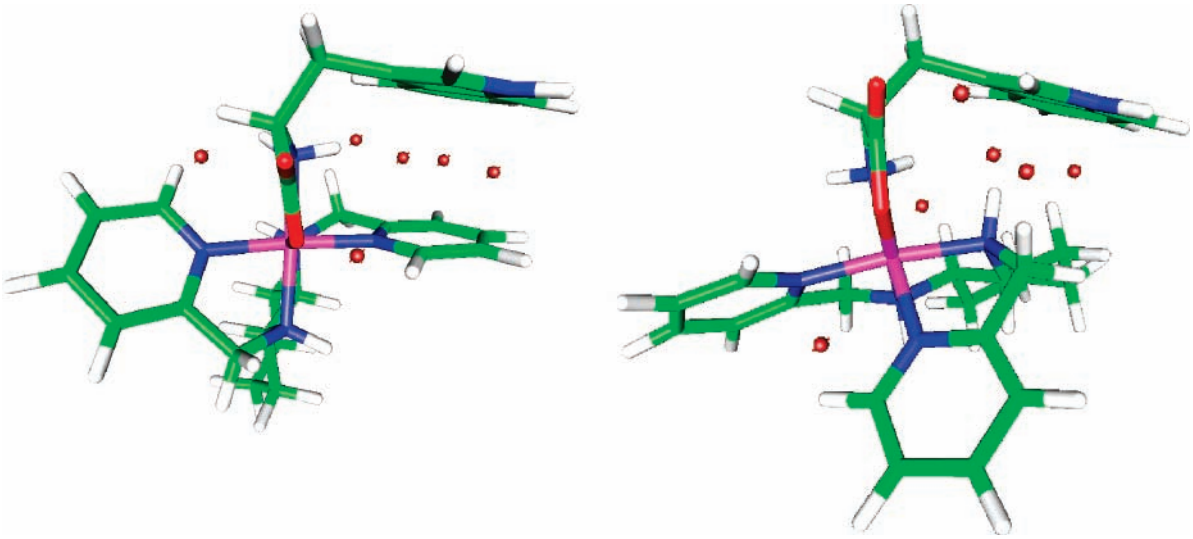

Figure 7. Intramolecular H-bond and π-stacking bcp's from DFT-calculated densities of **1** and **2**, indicating the presence of $\pi\cdots\pi$ stacking in the former and X− H$\cdots$,π interactions in the latter. (See text for more details.) BCPs are displayed as red spheres.

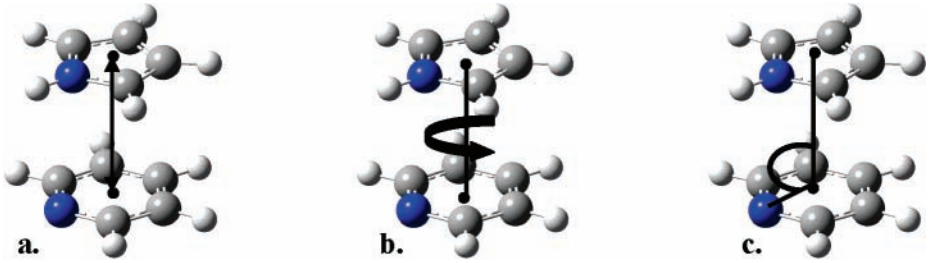

Figure 8. Pyrrole pyridine in parallel-displaced conformation (C_s symmetry): (a) intercentroid distance; (b) relative rotation of rings; (c) interplanar angle.

mol^{-1} to this value, C−H$\cdots\pi$ 3.5 kJ mol^{-1} and the single C−H$\cdots$O H-bond 7 kJ mol^{-1}. In **2**, X−H$\cdots\pi$ H-bonds contribute 16 kJ mol^{-1}, and the remaining H-bonds, 14 kJ mol^{-1}. Thus, these interactions account for approximately half of the total energy difference between isomers, though the differences in interactions between picchxn and the indole ring of tryptophan are rather smaller than this.

In addition to this electron density-based approach, we also constructed some small model systems to investigate these weak interactions. The weak $\pi\cdots\pi$ interaction observed in **1** was modeled by a system consisting of a stacked complex of pyridine and pyrrole, with ab initio calculations at the MP2/6-311++G-(d,p) level. Coordinates were extracted from the crystal structure, and no subsequent geometric optimization was performed. This yielded a counterpoise corrected binding energy of 8.40 kJ mol^{-1}, i.e., reasonably close to that estimated from density properties. Given the statistical error on estimation of stacking energies from BCP properties of 2 kJ mol^{-1} and the neglect of the environment of the rings in MP2 calculations, we believe this agreement to be rather fortuitous. Nonetheless, we conclude that the $\pi\cdots\pi$ interaction in **1** contributes approximately 10 kJ mol^{-1} to the overall energy.

To further explore this interaction (Figure 8), portions of the PES for the stacked pyridine−pyrrole system were calculated at the same MP2 level: in particular, we studied the intercentroid distance, interplanar angle, and relative rotation of rings. The interplane separation follows the expected Lennard-Jones shape, with a steep repulsive part at small separation and a shallow minimum at around 3.80 Å. The interplane separation in **1** is 3.79 Å, i.e., very close to the model system value. This small variation is perhaps surprising given the fairly shallow nature of the theoretically determined PES.

The rotation of pyrrole relative to pyridine (N(pyrrole)−ring centroid(pyrrole)− ring centroid(pyridine)−N(pyridine)) shows a rather flat PES, with the minimum energy orientation around 0° and maximum around 180° In **1**, this torsion has a value of approximately 120°, which corresponds to 5 kJ mol^{-1} more than the ideal orientation. In contrast, the PES for interplanar canting is noticeably steeper: the model system has minimum energy at 90°, while in **1** this value is found to be 94°, which is very close to the ideal gas-phase geometry. We suggest that these differences might be attributed to the steric restraints resulting from octahedral coordination around the cobalt center.

Complex **2** exhibits no $\pi\cdots\pi$-stacking, but our AIM analysis indicates the presence of N−H$\cdots\pi$ and C−H$\cdots\pi$ interactions. To model these, we used dimethylamine$\cdots$pyrrole and ethyl$\cdots$pyrrole and again carried out MP2/6-311++G(d,p) binding energy calculations.

We calculate a counterpoise corrected binding energy of 8.83 and 3.40 kJ mol^{-1} for the N−H$\cdots\pi$ interaction and C−H$\cdots\pi$ interaction, respectively, i.e., only slightly less than the AIM estimate reported above (Figure 9). This agreement between approaches is perhaps surprising, since in complex **2** the nitrogen is coordinated to Co, which might be expected to alter H-bonding properties of N−H. The fact that electron density and supermolecular-derived binding energies are so similar suggests that Co does not significantly assist this hydrogen bonding.

Energetics: Theory vs Experiment. We have estimated the strength of the π-stacking interactions in **1** and the X−H$\cdots\pi$ interactions in **2** in three separate ways: from the experimental EDD, from the theoretical EDD, and from theoretical supermolecule calculations. For **1**, these methods give the total energy of weak interactions as respectively 4.2, 12.9, and 8.4 kJ mol^{-1},

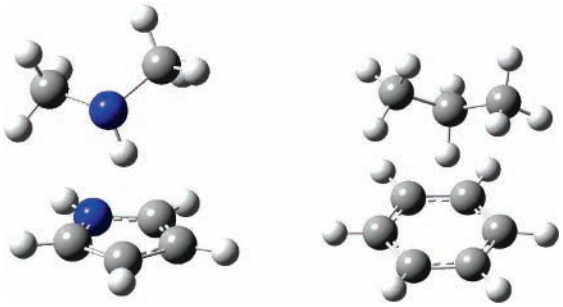

Figure 9. Left: Dimethylamine−pyrrole dimer as a model of N−H···π interaction. Right: Propane−benzene dimer as a model of C−H···π interaction.

while for **2** they yield 15.8, 15.7, and 12.2 kJ mol^{-1}. Agreement is therefore generally good, and given the statistical errors associated with the experimental and theoretical EDD methods (3 kJ mol^{-1}), the values for **2** are insignificantly different. Agreement between methods is less good for **1**: theoretical EDD and supermolecule approaches are in reasonable agreement, considering the likely errors in each method (discussed at length in ref 26). The experimental EDD value for π···π stacking energy of 4.2 kJ mol^{-1} is much less than either theoretical value. However, we note that the approach developed by Espinosa et al.[43] was originally intended for hydrogen bonding and has not been properly tested for these weaker, less directional interactions. This study represents the first attempt, as far as we are aware, to use experimental EDD determinations to estimate the strength of such weak, non-hydrogen-bonding interactions: our results suggest that much further work is required before this could be considered routine.

Density functional theory calculations reveal that **2** is 12 kJ mol^{-1} more stable than **1**. Theoretical approaches discussed above indicate that weak interactions contribute between 4 and 6 kJ mol^{-1} to this difference, while the experimental EDD data suggests that *all* of this difference could be ascribed to weak interactions. However, as discussed the stabilization of **1** may be underestimated, and hence, the energy difference overestimated using this method. Experimental and theoretical data show considerable differences in Co−ligand bond properties, but it is difficult to accurately relate such properties directly to bond energies. The above data suggest that, despite these large differences in bonding, the sum of bond energies in these isomers differs by only 6−8 kJ mol^{-1} at most.

Supermolecular calculations, which do not include cobalt, agree reasonably well with EDD-derived values, which implicitly contain the effects of cobalt. This indicates that the presence of the cobalt does not heavily perturb these weak interactions. Therefore, this combination of approaches is complementary, enabling a better understanding of weak interactions in these complexes.

Conclusions

The electron density distribution (EDD) of two isomeric cobalt complexes **1** and **2** have been analyzed and compared using of experimental and theoretical methods, allowing us to compare the electronic structure, metal−ligand bonding, and any weak noncovalent bonding between isomers. A broad similarity between EDDs of these complexes is evident, for example in Co−ligand bonds, the shape of the valence shell charge concentration (VSCC), and d-orbital populations of Co. However, some properties such as atomic charges and volumes appear to be more sensitive to the details of the environment. The transferability of electron density between isomers was tested in two separate ways; both measures suggest significant deviations from ideal transferability such that we conclude that this is invalid between these isomers. Weak interactions were probed using experimental and theoretical EDDs, which contain bond critical points corresponding to two π···π bcp's in **1** and two X−H···π bcp's in **2**. From these, we can estimate the interactions in **2** to be 10 kJ mol^{-1} stronger than in **1**. This analysis was supplemented by theoretical calculations of the electron density in the cations of **1** and **2** and of smaller model systems. All approaches agree that **2** is more stable than **1** and that this stability is due in large part to weak interactions rather than differences in metal−ligand bonding.

Acknowledgment. J.O. thanks the Danish Research Council for financial support for a postdoc position in Australia. M.P.W. acknowledges the AINSE postgraduate program and the University of Sydney for generous financial support. D.E.H. thanks the ARC for funding.

Supporting Information Available: Figures showing the potential energy dependence on the angle for canting and rotation, relating to Figure 8b,c, respectively, the output from program UIJXN for comparison of neutron and X-ray atomic displacement parameters for compound **2**, a complete topological analysis of the experimental electron density of both **1** and **2**, theoretical data for Co−ligand bonds in **1** and **2**, a full citation for ref 22, experimental details of charge density refinement, and CIF files for both compounds. This material is available free of charge via the Internet at http://pubs.acs.org.

References and Notes

(1) (a) Adams, H.; Carver, F. J.; Hunter, C. A.; Osborne, N. J. *Chem. Commun.* **1996**, 2529. (b) Levit, M.; Prutz, M. F. *J. Mol. Biol.* **1988**, *201*, 751. (c) Armstrong, K. M.; Fairman, R.; Baldwin, R. L. *J. Mol. Biol.* **1993**, *230*, 284.

(2) (a) Babine, R. E.; Bender, S. L. *Chem. Rev.* **1997**, *97*, 1359. (b) Liu, S.; Gilliland, G. L.; Stevens, W. J.; Armstrong, R. N. *J. Am. Chem. Soc.* **1993**, *115*, 7910.

(3) Emseis, P.; Failes, T. W.; Hibbs, D. E.; Leverett, P.; Williams, P. A. *Polyhedron* **2004**, *23*, 1749−1767.

(4) (a) Lindoy, L. F.; Atkinson, I. M. In *Monographs in Supramolecular Chemistry*; Stoddart, J. F., Ed.; The Royal Society of Chemistry: Cambridge, U.K., 2000; Vol. 7, pp 7−46 and references therein. (b) Phillip, D.; Stoddart, J. F. *Angew. Chem., Int. Ed.* **1996**, *35*, 1154 and references therein.

(5) Anderson, M. A.; Birse, E. F.; Hewlins, M. J. E.; Richards, J. P. G.; Stephens, F. S.; Vagg, R. S.; Williams, P. A. *Inorg. Chem.* **1991**, *30*, 3774.

(6) Madsen, A. Ø.; Sørensen, H. O.; Flensburg, C.; Stewart, R. F.; Larsen, S. *Acta Crystallogr., Sect. A* **2004**, *60*, 550−561.

(7) (a) Stewart, R. F. *Isr. J. Chem.* **1969**, *51*, 4569−4577. (b) Hansen, N. K.; Coppens, P. *Acta Crystallogr., Sect. A* **1979**, *39*, 909−921.

(8) Bader, R. F. W. *Atoms in Molecules: A Quantum Theory*; Clarendon Press: Oxford, U.K., 1990. Popelier, P. L. A. *Atom in Molecules. An Introduction*; Pearson Education: Harlow, U.K., 1999.

(9) Bader, R. F. W.; Larouche, A.; Gatti, C.; Carroll, M. T.; MacDougall, P. J.; Wiberg, K. B. *J. Chem. Phys.* **1987**, *87*, 1142−1152. Matta, C. F.; Bader, R. F. W. *Proteins* **2003**, *52*, 360−399.

(10) Jelsch, C.; Pichon-Pesme, V.; Lecomte, C.; Aubry, A. *Acta Crystallogr., Sect. D* **1998**, *54*, 1306−1318. Jelsch, C.; Teeter, M. M.; Lamzin, V.; Pichon-Pesme, V.; Blessing, R. H.; Lecomte, C. *Proc. Natl. Acad. Sci. U.S.A.* **2000**, *97*, 3171−3176.

(11) Pichon-Pesme, V.; Lecomte, C.; Lachekar, H. *J. Phys. Chem.* **1995**, *99*, 6242−6250. Efforts have been made to produce a database from theoretical calculations: Volkov, A.; Li, X.; Koritsanszky, T.; Coppens, P. *J. Phys. Chem. A* **2004**, *108*, 4283−4300.

(12) Cox, M. A.; Goodwin, T. J.; Jones, P.; Williams, P. A.; Stephens, F. S.; Vagg, R. S. *Inorg. Chim. Acta* **1987**, *127*, 49.

(13) *SAINT+. Program to Integrate and Reduce Raw Crystallographic Area Detector Data*; Siemens AXS: Madison, WI, 2001.

(14) Blessing, R. H. *J. Appl. Crystallogr.* **1997**, *30*, 421−426.

(15) Farrugia, L. J. *J. Appl. Crystallogr.* **1999**, *32*, 837−838.

(16) Emseis, P. Ph.D. Thesis, University of New South Wales, NSW, Australia, 2003.

(17) Sheldrick, G. M. *SHELX97-Programs for Crystal Structure Analysis*, release 97-2; Institüt für Anorganische Chemie der Universität: Tammanstrasse 4, D-3400 Göttingen, Germany, 1998.

(18) Blessing, R. H. *Acta Crystallogr., Sect. B* **1995**, *51*, 816−823.

(19) Koritsanszky, T.; Howard, S. T.; Richter, T.; Mallinson, P. R.; Su, Z.; Hansen, N. K. *XD. A Computer Program Package for Multipole Refinement and Analysis of Charge Densities from X-ray Diffraction Data*; Free University of Berlin: Berlin, Germany, 1995.

(20) Su, Z.; Coppens, P. *Acta Crystallogr., Sect. A* **1998**, *54*, 646−652.

(21) Hirshfeld, F. L. *Acta Crystallogr.* **1976**, *A32*, 239−244.

(22) Frisch, M. J.; et al. *Gaussian 03*; Gaussian, Inc.: Pittsburgh, PA, 2003 (see Supporting Information for full reference).

(23) Becke, A. D. *J. Chem. Phys.* **1993**, *98*, 1372.

(24) Hehre, W. J.; Ditchfie, R.; Pople, J. A. *J. Chem. Phys.* **1972**, *56*, 2257. Frisch, M. J.; Pople, J. A.; Binkley, J. S. *J. Chem. Phys.* **1984**, *80*, 3265.

(25) Dolg, M.; Wedig, U.; Stoll, H.; Preuss, H. *J. Chem. Phys.* **1987**, *86*, 866.

(26) Waller, M. P.; Robertazzi, A.; Hibbs, D. E.; Williams, P. A.; Platts, J. A. *J. Comput. Chem.* **2006**, *27*, 491−504.

(27) http://www.chemistry.mcmaster.ca/bader/aim/.

(28) Friedrich, Biegler-Konig, J. S. *J. Comput. Chem.* **2002**, *23*, 1489.

(29) Volkov, A.; Gatti, C.; Abramov, Y.; Coppens, P. *Acta Crystallogr., Sect. A* **2000**, *56*, 252−258.

(30) Holladay, A.; Leung, P.; Coppens, P. *Acta Crystallogr., Sect. A* **1983**, *39*, 377−387. Note that the sum of the d-orbital populations is constrained to equal the total valence population, P_{00}.

(31) Sabino, J. R.; Coppens, P. *Acta Crystallogr., Sect. A* **2003**, *59*, 127−131.

(32) Crabtree, R. H. *The Organometallic Chemistry of the Transition Metals*; John Wiley & Sons: New York, 1994.

(33) (a) Cremer, D.; Kraka, E. *Angew. Chem., Int. Ed.* **1984**, *23*, 627−628. (b) Cremer, D.; Kraka, E. *Croat. Chem. Acta* **1984**, 1259.

(34) Abramov, Yu. A. *Acta Crystallogr., Sect. A* **1997**, *53*, 264−272.

(35) In their work, Macchi et al. addressed the nature of both metal−ligand bonds and metal−metal interactions: Macchi, P.; Garlaschelli, L.; Sironi, A. *J. Am. Chem. Soc.* **2002**, *124*, 14173−14184. Macchi, P.; Proserpio, D. M.; Sironi, A. *J. Am. Chem. Soc.* **1998**, *120*, 13429−13435. However, some controversy persists in relation to the existence of a metal−metal bent bond: Finger, M.; Reinhold, J. *Inorg. Chem.* **2003**, *42*, 8128−8130.

(36) Coppens, P. *X-ray Charge Densities and Chemical Bonding*; Oxford University Press: Oxford, U.K., 1999.

(37) To estimate the reliability of the surface determination, the integrated Laplacian is used. In theory, this property should vanish and its value can therefore be used as an indication of the quality of the integrated charges. For all atoms the value of the integrated Laplacian is below 10^{-3}, showing that the charges and volumes are reliable.

(38) Reed, A. E.; Curtiss, L. A.; Weinhold, F. *Chem. Rev.* **1988**, *88*, 899.

(39) The full list of multipole parameters is available in the Supporting Information. It should be noted that it is imperative in this comparison that the local coordinate systems used in the description of the population parameters are defined in complete agreement between systems.

(40) El Haouzi, A.; Hansen, N. K.; Le Henaff, C.; Protas, J. *Acta Crystallogr., Sect. A* **1996**, *52*, 291−301.

(41) Popelier, P. L. A. *J. Phys. Chem. A* **1999**, *103*, 2883−2890. O'Brien, S. E.; Popelier, P. L. A. *J. Chem. Inf. Comput. Sci.* **2001**, *41*, 764−775.

(42) Matta, C. F.; Hernandez-Trujillo, J.; Tang, T.-H.; Bader, R. F. W. *Chem.—Eur. J.* **2003**, *9*, 1940.

(43) Espinosa, E.; Lecomte, C.; Molins, E. *Chem. Phys. Lett.* **1999**, *300*, 745−748. Espinosa, E.; Alkorta, I.; Elguero, J.; Molins, E. *J. Chem. Phys.* **2002**, *117*, 5529−5542.